

Control of broadband optically generated ultrasound pulses using binary amplitude holograms^{a)}

Michael D. Brown,^{1,b)} Jiri Jaros,² Ben T. Cox,¹ and Bradley E. Treeby¹

¹Department of Medical Physics and Biomedical Engineering, University College London,

2-10 Stephenson Way, NW1 2HE London, United Kingdom

²Faculty of Information Technology, Brno University of Technology, Bozetechova 2, 612 66 Brno, Czech Republic

(Received 15 September 2015; revised 26 February 2016; accepted 11 March 2016; published online 6 April 2016)

In this work, the use of binary amplitude holography is investigated as a mechanism to focus broadband acoustic pulses generated by high peak-power pulsed lasers. Two algorithms are described for the calculation of the binary holograms; one using ray-tracing, and one using an optimization based on direct binary search. It is shown using numerical simulations that when a binary amplitude hologram is excited by a train of laser pulses at its design frequency, the acoustic field can be focused at a pre-determined distribution of points, including single and multiple focal points, and line and square foci. The numerical results are validated by acoustic field measurements from binary amplitude holograms, excited by a high peak-power laser.

© 2016 Author(s). All article content, except where otherwise noted, is licensed under a Creative Commons Attribution (CC BY) license (<http://creativecommons.org/licenses/by/4.0/>).

[<http://dx.doi.org/10.1121/1.4944758>]

[JDM]

Pages: 1637–1647

I. INTRODUCTION

The photoacoustic effect occurs when a time varying optical source, which can be coherent or incoherent, is incident on an optically absorbing material. The incident photons are absorbed and converted to heat by non-radiative de-excitation. This causes a small temperature rise resulting in local pressure increase which generates an acoustic pulse.¹ Within the past decade there has been increasing interest in optically generated ultrasound (OGUS) for biomedical applications due to a steady increase in the acoustic pressures that can be generated. This is principally due to the development of materials with higher photoacoustic efficiencies.² For example, nano-composites composed of separate elastomeric and absorbing components possessing high optical absorption, efficient heat transduction, and high thermal expansion have been used to generate focused pressures of 50 MPa.³ OGUS has several clear advantages compared to piezoelectrics. These include very wide bandwidths of 100s of MHz,⁴ non-contact excitation, and flexible element size.⁵ In addition, by controlling both the optical pulse shape and spatial illumination pattern to a two-dimensional (2-D) absorber, it is possible to achieve a high degree of control over the resulting acoustic field in three dimensions, without the drawbacks associated with 2-D capacitive micromachined ultrasonic transducer (CMUT)⁶ and piezoelectric arrays.⁷

One configuration for the optical generation of ultrasound uses a laser and a thin layer of a highly absorbing material. The laser pulse is first expanded, then absorbed by the

layer where it generates a plane wave.⁵ By controlling the spatial pattern of optical energy incident on the absorber, the resulting acoustic pulse can be focused or particular frequencies excited. For example, generating an annular pattern using an axicon lens^{8,9} or spatial light modulator (SLM)¹⁰ results in a more intense acoustic signal at the center of the ring. Alternatively, generating a stationary fringe by interfering two laser pulses,¹¹ or a moving fringe by interfering two frequency shifted laser pulses¹² results in an acoustic pulse with peaks in its spectra determined by the fringe spacing. An equivalent effect can also be achieved by patterning the absorbing layer. The initial distribution of pressure is then controlled by absorption differences over this layer. Both diffraction gratings and Fresnel zone plates (FZPs) have been manufactured in this way for applications using surface^{13,14} and longitudinal waves,¹⁵ respectively.

By controlling the temporal application of the optical radiation to the absorber, the spectrum of the resulting pulse can be further controlled. For example, a single short optical pulse can excite an acoustic pulse with a broadband spectrum.⁴ Using multiple short optical pulses with an even temporal spacing results in an acoustic signal with a spectrum possessing peaks at the pulsing repetition frequency (PRF) and at harmonics contained in the initially broadband spectrum.¹⁶ Alternatively, if the optical intensity is modulated sinusoidally, the resulting acoustic spectrum has a single peak at the modulation frequency.^{17,18}

Both spatial and temporal modulation have been combined in several works. Sharples *et al.* used a mode locked Q-switched laser that generated 30 pulses with a spacing of 12.1 ns to excite surface acoustic waves.¹⁹ The pulses produced by this laser were patterned with an SLM into a series of concentric arcs. By matching the acoustic transit time

^{a)}Portions of this work were presented in "Control of Optically Generated Ultrasound Fields Using Binary Amplitude Holograms," IEEE International Ultrasonics Symposium, Chicago, IL, September 2014.

^{b)}Electronic mail: michael.brown.13@ucl.ac.uk

between neighboring arcs to the repetition rate of the laser, the amplitude at the focus was maximized. Meyer *et al.*¹⁸ modulated the intensity of a 10 μ s 550 mJ laser pulse to vary sinusoidally such that it excited narrowband acoustic tone bursts.²⁰ The spatial intensity or relative phase of the laser pulse was then also modulated using an SLM. The result was a 2-D acoustic pulse with a predetermined frequency and spatial pattern. The 3-D acoustic field could then be controlled using binary amplitude or phase holography. The resulting system was used to generate several novel acoustic patterns including a line and an annular focus.

Accurate spatial control of optically generated acoustic fields is therefore possible for narrowband pulses by using holographic patterns to control where the acoustic waves constructively interfere. However, it is difficult to achieve high acoustic pressures (e.g., those needed in biomedical ultrasound) using this approach due to lower peak powers of these optical sources. For example, the pressures reported in Ref. 20 were limited to \sim 10 kPa. One approach to overcome this limitation is to use short duration high peak power pulses from a Q-switched laser. These lasers have significantly greater peak-powers so have the potential to generate much higher acoustic pressures. Spectral control of the acoustic field can be achieved by the use of multiple pulses applied with a high PRF (MHz). This could enable optically generated ultrasound to become a practical modality for 2-D ultrasound arrays. However, consideration also needs to be given to the optimal design of binary holograms for this application.

In this work, the properties of the acoustic fields that can be generated by the use of pulsed lasers and binary amplitude holograms are explored in detail. The first section investigates numerically the acoustic fields generated by binary amplitude holograms with a single focus, establishing the experimental conditions influencing the generation of a focus. In the second section, this is extended to binary amplitude holograms with multiple foci, exploring their possibilities and limitations. The third section validates the numerical model and demonstrates that this approach can be applied experimentally with the use of patterned optical absorbers and a Q-switch laser.

II. SINGLE FOCUS HOLOGRAMS

A. Computer generated binary amplitude holograms

A binary amplitude hologram is a 2-D binary pattern designed to control the distribution of light or sound of a particular wavelength in three dimensions. Pixels that are “on” in the pattern transmit waves which constructively interfere at the design points. Pixels that are “off” do not transmit.

A ray-based algorithm was implemented for the calculation of binary amplitude holograms designed to generate a single acoustic focus. For each hologram, a target point, aperture size (i.e., hologram size), pixel size (i.e., the size of a hologram element), and design wavelength are defined. The pressure $p(x, y)$ on the surface of the 2-D hologram is then calculated by approximating the focal point as a monochromatic point source oscillating at the design frequency, where

$$p(x, y) = Re \left\{ \frac{1}{r} e^{ikr + \Phi} \right\}. \quad (1)$$

Here r is the distance from the focal point to each position on the hologram surface, k is the wavenumber at the design frequency f (where $k = 2\pi f/c$, and c is the soundspeed), and Φ is an arbitrary phase offset (the effect of which is discussed further in Sec. II F). The calculated 2-D pressure on the hologram surface is then thresholded with positive values of $p(x, y)$ set to 1 and negative values set to 0 to produce a binary hologram. An example hologram is plotted in Fig. 2. For the holograms depicted in this work, black pixels are “on” and white pixels are “off.”

A binary amplitude hologram with a single focus is known as a FZP. A FZP consists of a series of alternating dark and light rings. The path length difference to the focus from neighboring rings differs by half a wavelength of the design frequency. It is possible to derive an expression for one set of radii for the center of each “on” ring of a FZP with a focus at depth d from Eq. (1) by setting $\Phi = (-2\pi d)/\lambda$, which yields

$$l_n = \sqrt{2n\lambda d + n^2\lambda^2}. \quad (2)$$

Here l_n is the radii of the n th ring on the zone plate, d is the focal depth, and λ is the design wavelength. For most FZP $\lambda \ll d$, so for small n , Eq. (2) can be approximated by

$$l_n \approx \sqrt{2n\lambda d}. \quad (3)$$

In addition to the main focus, FZP’s have several less intense higher order foci along the main axis corresponding to points where the path length difference is $n\lambda$ for odd n . These occur at distances of approximately d/n .

B. Hologram acoustic field simulations

The acoustic fields generated by binary amplitude holograms when excited by a set of laser pulses spaced at their design frequency were simulated using the k-Wave toolbox.^{22,23} This uses a k-space pseudo-spectral model for time domain simulations of acoustic waves. For all simulations the medium was homogeneous with a density of 1000 kg m^{-3} and a sound speed of 1500 m s^{-1} . Unless otherwise stated the simulations were carried out on a regular $512 \times 512 \times 512$ Cartesian grid with a grid point spacing of 25 μ m, time steps of 5 ns, and a maximum supported frequency of 30 MHz. The thickness of the perfectly matched layer was set to ten grid points. Holograms were inserted at one edge of the simulation domain as a source mask. Laser pulses incident on the absorber were represented temporally as impulses at discrete simulation time points inserted at the nearest point to the analytic pulsing frequency. The temporal input was filtered at 30 MHz to remove frequencies not supported by the spatial grid.

C. Pulsed acoustic sources vs monochromatic

The calculation of a binary amplitude hologram using Eq. (1) assumes a monochromatic input spectrum. In

comparison, the spectrum of the acoustic wave generated by a short optical pulse is broadband or, if generated at a set repetition rate, has peaks at the PRF and harmonics of the PRF contained in the broadband spectrum of the single pulse.

To establish the effect the difference between the assumed spectra and the actual spectra has on the resulting field, the monochromatic and pulsed inputs were compared in simulation. A hologram was calculated for a design frequency of 5 MHz, with a 0.03 mm pixel spacing, a $1.5 \text{ cm} \times 1.5 \text{ cm}$ aperture, and a focus at 1.5 cm. The fields generated from this hologram were simulated on a $540 \times 540 \times 1536$ grid, with a grid spacing of 0.03 mm. The maximum supported frequency was 25 MHz. The hologram was inserted as a source distribution in the (x, y) plane along the edge of the grid. The two optical inputs were represented in the simulation using a sinusoid (for the monochromatic input), and using a train of delta functions spaced at 5 MHz (to represent a pulsed laser input). Figure 1(a) shows the maximum amplitude projection (MAP) of the peak pressure in each voxel of the hologram field generated with a pulsed laser input. Figure 1(b) is the MAP of the same field generated by a monochromatic input.

There are several significant differences introduced by the harmonics in the acoustic spectrum. First, the volume of the design focus labeled f_0 in both figures, measured by thresholding the maximum pressure data at 50% of the overall maximum, is reduced by 92% compared to the monochromatic input. Second, the signal to noise of the focus relative to the background is decreased. Third, there are several additional foci present in the pulsed field not present in the monochromatic field. These are generated by the harmonics in the source spectrum. From Eq. (3) it can be seen that halving the wavelength λ and keeping the radii constant approximately doubles the focal length d . Therefore, the hologram focuses each harmonic at a point further away from the hologram aperture. As with the fundamental, each

harmonic also generates higher order foci at points where the path length from subsequent rings differs by an odd number of wavelengths of that harmonic, an example is labeled in Fig. 1(a) as $f_4/3$. This is the third order foci for the fourth harmonic. Certain higher order foci of odd harmonic frequencies also spatially coincide with the design focus, for example, $f_3/3$. This spatial overlapping is responsible for the reduction in focus volume observed in the pulsed input relative to the monochromatic input.

D. Zone plate resolution and pulse number

To understand the parameters required to represent a hologram and generate an axial focus, the effect of resolution (pixel size) and the number of laser pulses on the focus volume and peak pressure was investigated. Simulations were carried out using four equivalent holograms calculated with resolutions of $\lambda/16$, $\lambda/8$, $\lambda/4$, and $\lambda/2$ relative to the design frequency of 3.75 MHz. Each hologram had a $1 \text{ cm} \times 1 \text{ cm}$ aperture and a focus at a depth of 1 cm. For each hologram, 15 simulations were carried out increasing the number of pulses applied from 1 to 15. The volume of the focus was evaluated in each simulation by thresholding the maximum pressure at each simulation voxel at 50% of the maximum pressure at the focus then calculating the number of voxels in the cluster containing the target focus point.

As shown in Fig. 2(b), the volume of the focus decreases with each additional pulse, reaching a steady state for each hologram at approximately six pulses, which matches the number of rings on the hologram. It is also the point where the temporal spacing between the first and last pulses in the input signal matches the travel time difference between waves from the edge and center of the hologram to the focus. The largest decrease in focal volume is seen between the one and two pulse inputs. This is because for a single pulse the acoustic field is not axially focused as

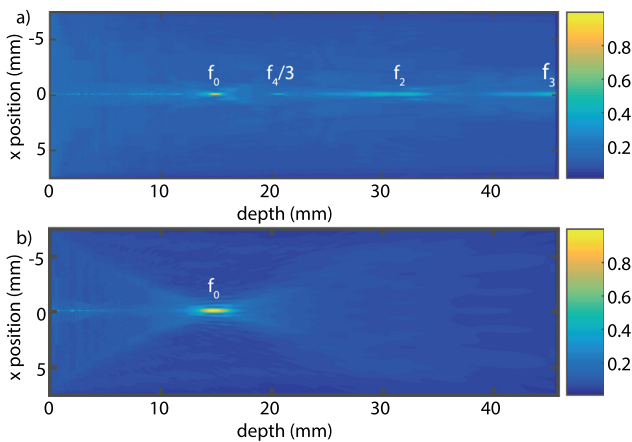


FIG. 1. (Color online) (a) Maximum amplitude projection (MAP) of maximum pressure generated by the hologram with a pulsed input, normalized to peak pressure in simulation. (b) MAP of maximum pressure generated by the hologram with a monochromatic input, normalized to peak pressure in simulation. The pulsed input generates a lower focus volume but also generates several additional foci and has lower signal to noise.

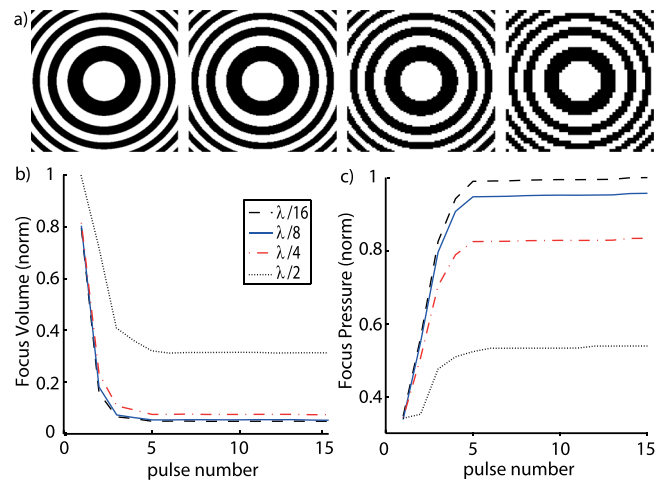


FIG. 2. (Color online) (a) Four holograms used in the simulations. The resolutions from left to right are $\lambda/16$, $\lambda/8$, $\lambda/4$, and $\lambda/2$. (b) Variation in focus volume with number of pulses applied in the simulation for each hologram. (c) Variation in maximum pressure at the focus with number of pulses for each hologram. Maximum pressure increases and focus volume decreases with increasing hologram resolution and increasing pulse numbers.

there is no temporal overlap between the acoustic signal from different rings. For two or more pulses the acoustic signal from neighboring rings can constructively interfere generating a focus. The volume of the focus at any given pulse number decreases with increasing hologram resolution. However, the fractional improvement reduces with each subsequent increase in resolution, e.g., a gain of only $\sim 8\%$ is seen between the $\lambda/8$ and $\lambda/16$ holograms. Similar trends are observed for maximum pressure as shown in Fig. 2(c).

The spacing between rings on a zone plate, and their width, decreases with increasing distance from the center [this can be seen in Figs. 4(c) and 4(d)]. This means both the resolution required to represent the zone plate and the number of pulses needed for the field to converge will increase with increasing aperture size. Both parameters will also vary depending on the depth of focus relative to the aperture and if the focus is moved off the hologram center. However, the simulations demonstrate that a focus can be generated with a relatively low hologram resolution $\sim \lambda/2$ (corresponding to $75 \mu\text{m}$ for 10 MHz), and with as few as two optical pulses.

E. Optical pulsing frequency

After establishing the conditions required for convergence of the field from a particular hologram, the degree to which the acoustic field of individual holograms can be varied was considered. The focal length of a hologram varies depending on the input frequency. As the spectrum generated by a train of optical pulses is determined by the PRF, it should be possible to vary the axial focus position by altering the PRF.

A prediction of the focal depth of each ring on the hologram can be calculated by inverting Eq. (2),

$$d_n = \frac{l_n^2}{2n\lambda} - \frac{n\lambda}{2}. \quad (4)$$

Here d_n is the prediction for the focal depth from the n th radii. By substituting in the appropriate wavelength and taking the average of d_n this gives a prediction of the focus depth for each PRF.

To validate Eq. (4) its predictions were compared against simulations. A hologram was calculated for a design frequency of 9 MHz, with a $0.75 \text{ cm} \times 0.75 \text{ cm}$ aperture, and a focus at 0.75 cm. The fields generated by this hologram were simulated altering the PRF between 4.5 MHz and 13.5 MHz. For each simulation the input source was filtered at 2.2 points per wavelength (PPW) relative to the pulsing frequency and the magnitude was normalized. The focus position was recorded in each simulation as the depth from the hologram at which the peak pressure occurred. The peak pressure and lateral FWHM of the focus (beamwidth) were also both evaluated.

Figure 3(a) shows the measured variation in focus depth with pulsing frequency compared to the prediction from Eq. (4). The two are in close agreement. Figure 3(b) shows the variation in peak pressure and beamwidth at the focus as a function of pulsing frequency. With increasing pulsing

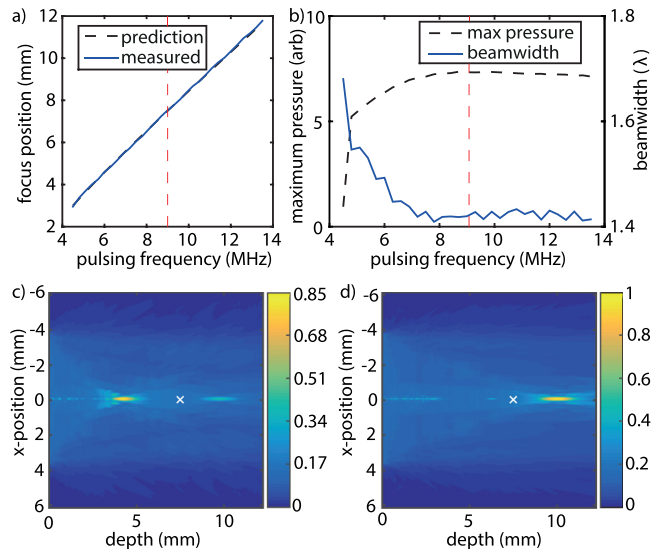


FIG. 3. (Color online) (a) Variation in focus depth with pulsing frequency, as measured in simulation and predicted by Eq. (4). The simulated data and the prediction show good agreement. (b) Variation in peak pressure and focus width with pulsing frequency. The dotted lines in (a) and (b) indicate the design frequency of 5.7 MHz. (c) MAP of the maximum pressure field for a pulsing frequency of 5.7 MHz. Pressure is normalized relative to maximum in (d). (d) MAP of the maximum pressure field for a pulsing frequency of 11.7 MHz. The crosses in (c) and (d) indicate the position of the target focus at 9 MHz.

frequency compared to the design, the pressure at the focus and the beamwidth remain approximately constant. Conversely, as the pulsing frequency drops, the peak pressure lowers and the beamwidth increases. One possible cause is that the variation in the focus depth predicted by different rings becomes larger as the pulsing frequency decreases. At much lower pulsing frequencies the focus is observed to split into a series of smaller foci at different depths. This is accompanied by a large drop in peak pressure. MAPs of the maximum pressure recorded in each voxel of the simulation are shown in Figs. 3(c) and 3(d) for pulsing frequencies of 5.7 and 11.7 MHz. These demonstrate the change in focus position.

F. Zone plate phase offset

A series of zone plates with identical focusing parameters but with rings at different positions can be generated by varying the phase offset Φ in Eq. (1). It has been found for optical zone plates that the choice of this parameter can influence the magnitude generated at both the focus and side lobes.²⁴ To test the impact of this parameter for acoustic holograms, a set of 60 equivalent holograms were generated by varying Φ between 0 and 2π . Each hologram had a design frequency of 9 MHz, a $1 \text{ cm} \times 1 \text{ cm}$ aperture and a focus at 1 cm. The acoustic field generated by each hologram was simulated with the application of 2, 4, and 40 pulses. The measured variation in beamwidth and maximum pressure are shown in Fig. 4.

For two pulses, the variation in beamwidth between the best and worst phase offset is 66% [Fig. 4(a)]. As the number of pulses used increases, a similar trend is observed, however, the fractional variation between the best and worst case decreases. For 40 pulses, where the field has reached steady

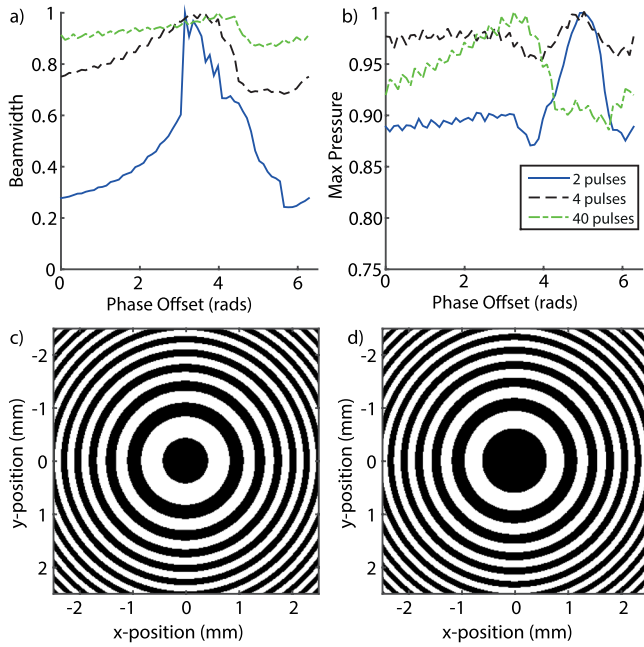


FIG. 4. (Color online) (a) Variation in beamwidth with choice of phase offset Φ for simulations using 2, 4, and 40 pulses, each normalized against the largest beamwidth. (b) Variation in maximum pressure at the focus with choice of phase offset for simulations using 2, 4, and 40 pulses, each normalized against the overall maximum pressure. (c) Hologram that generated smallest focal width with the application of 40 pulses. (d) Hologram that generated the largest focal width with the application of 40 pulses.

state, a variation of 9% occurs. From Figs. 4(c) and 4(d) it can be seen that the beamwidth is maximized when the area of the hologram's central region is large and active, and is minimized for a small active central region. This is also the case, with small variations, for lower pulse numbers, before the field has reached steady state. The peak simulation pressure is also seen to change with phase offset, however, the measured variation is low compared to that seen in the beamwidth [Fig. 4(b)]. The choice of Φ therefore has a significant impact on the resulting acoustic field.

III. MULTI-FOCI HOLOGRAMS

A. Computer generated holograms: Direct binary search

Having established the properties of the acoustic fields generated by binary amplitude holograms with a single design focus, the properties of holograms that target multiple distinct points and continuous patterns were investigated. Binary amplitude holograms with multiple focal points can be generated using the ray-based algorithm. This is done by evaluating the pressure $p(x, y)$ generated by each target point over the hologram using Eq. (1) separately, then superimposing the contribution of each point and thresholding the resulting pressure at 0. However, the acoustic fields generated by these holograms show large variations in pressure generated at different target points.

An example of this is given in Fig. 5. In Fig. 5(a) a hologram calculated to focus over the outline of a square is shown. The acoustic field generated by this hologram is plotted in Fig. 5(b). The acoustic field is significantly more

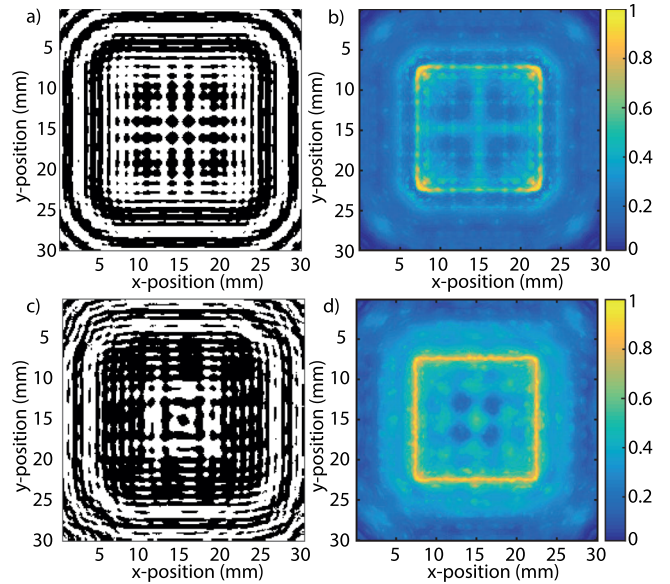


FIG. 5. (Color online) (a) Binary hologram designed to focus over the outline of a 1.5 cm square, in a plane 3 cm from the hologram. Hologram was calculated for a frequency of 3 MHz using the ray-based algorithm. (b) Maximum pressure in target plane of square generated by the hologram in (a) when simulated. (c) Binary hologram calculated for the same target points and frequency as the hologram in (a) using the direct binary search algorithm. (d) Maximum pressure in target plane of square generated by the hologram in (c) when simulated. The optimization algorithm produces a significantly better representation of the target pressure.

intense at the corners of the square, which makes the outline of the square difficult to resolve. This effect is due to the quantization of the hologram. For optical holograms, it has been previously found that binarization of the output of ray-based algorithms generates holograms that produce greater intensity along edges and corners and significantly lower intensities from other areas of the target pattern.²⁵

As a result an optimization approach was developed for the calculation of holograms with multiple foci. The hologram is initialized in a randomized binary state. The cost associated with this state is evaluated using a cost function first used by Clark in the design of binary optical phase holograms.²⁶ This is given by

$$C = -|\bar{p}| + \alpha\sigma, \quad (5)$$

where $|\bar{p}|$ is the average magnitude of the complex pressure at the target points, σ is the standard deviation of the pressure over the target points, and α is a factor weighting the two terms. Empirically a value between 1 and 2 for α was found to provide a good balance between maximizing the pressure at each target point and minimizing the variation. The pressure at each focal point is evaluated using the Rayleigh-Sommerfeld integral, that is,

$$p = \iint H(x, y) \frac{e^{ikr}}{r} dx dy. \quad (6)$$

Here $H(x, y)$ is the value of the hologram at the point (x, y) , and r is the distance from the (x, y) pixel to the focal point. The optimization then proceeds via direct binary search, first used by Seldowitz *et al.*²⁷ The state of single pixels are

flipped, the change in cost is evaluated, and the new state kept if it decreased. Pixels are chosen randomly, with each pixel on the hologram being explored once before repeat tests. This continues until the number of changes that occur in an iteration is less than 0.01% of the overall number of pixels. The random-exhaustive approach to pixel selection was found to converge more rapidly than ordered or non-exhaustive selection. The random initialization and ordering of the pixel selection means the algorithm converges to different holograms between model runs. However, the differences in the acoustic fields generated by these holograms over the points of interest was found to be small ($<0.5\%$). A summary of the algorithm is shown in Fig. 6.

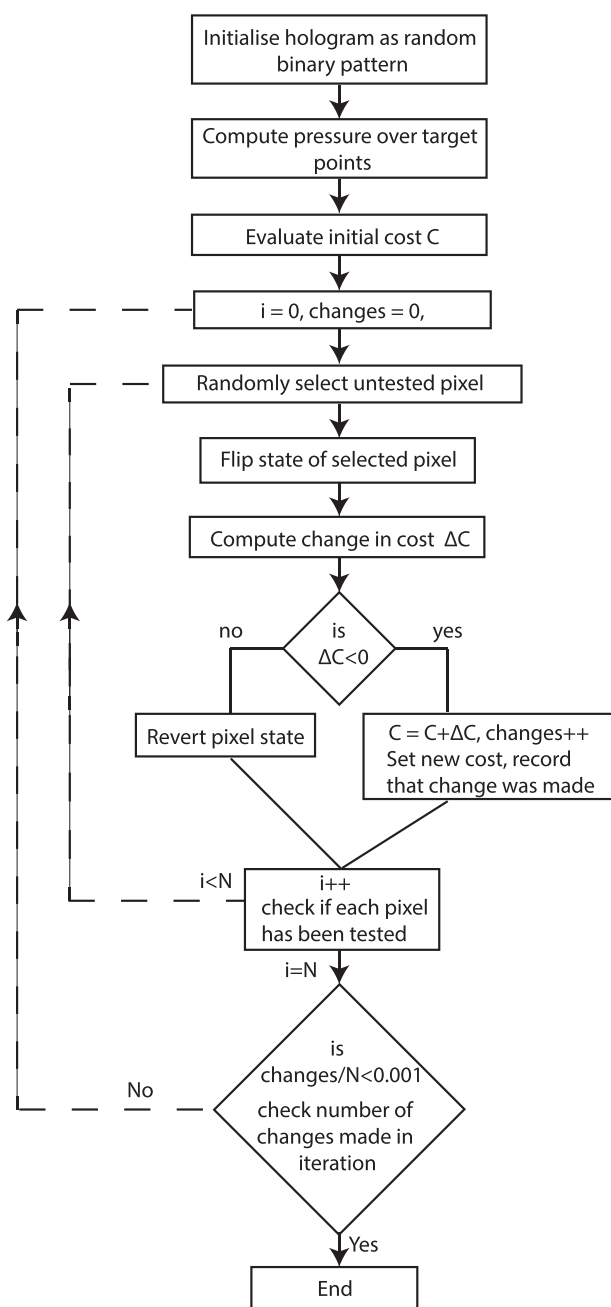


FIG. 6. Flow chart summarizing the optimization algorithm used in generating multi-foci holograms.

The optimization approach offers significant flexibility over the resulting holograms. Additional terms can be added to the cost function to control the acoustic field in different ways. For example, arbitrary weightings can be included to vary the pressure at different focal points, or the relative phase at different target points can be controlled.

Figures 5(c) and 5(d) show the hologram and acoustic field that result from applying the optimization algorithm to the same problem of generating the outline of a square. In this case, the square can be clearly resolved relative to the background, and the pressure is significantly more uniform.

B. Multi-foci holograms simulation parameters

Two further cases were investigated as a test of multi-foci holograms: an acoustic field with a line focus, and a field with a square array of foci. These were used to investigate the sampling rate needed to represent a continuous shape, and the change in pressure and foci size as a field is made to focus at several points. Simulations were carried out on a $256 \times 256 \times 256$ grid, with a grid spacing of 0.167 mm, time steps of 33 ns, and a maximum supported frequency of 4.5 MHz. Holograms were calculated for a design frequency of 3 MHz, over an aperture of 3.33 cm.

C. Line focus

The generation of a continuous pattern of pressure was investigated first. The target used was a line focus, 1.66 cm in length in a plane 3.33 cm from and parallel to the hologram aperture. As an input to the optimization algorithm, the line had to be discretized into a set of points. The spacing of these points was varied between 33.3λ to 0.168λ , and a hologram was generated for each spacing. The acoustic field generated by each hologram was simulated recording the average peak pressure in each voxel of the line, the variation in peak pressure over the line, and the peak pressure at each target point. These are each plotted in Fig. 7.

From Fig. 7(c) it can be seen that it is possible to generate an acoustic field focused over a line. The average maximum pressure over this line increases with decreasing point spacing until this spacing is less than $\sim 0.75\lambda$, at which point it remains stable showing only small variations between different point densities [Fig. 7(a)]. The maximum pressure at each individual foci decreases with decreasing point spacing until approximately 0.75λ , at this point it remains stable and matches the value of the average line pressure. As this spacing also coincides with a large drop in the variation of maximum pressure over the line, this demonstrates that 0.75λ is the maximum point spacing that can produce a continuous pattern without significant variations in pressure. For more sparse distributions the line is realized as a set of discrete foci [Fig. 7(b)].

D. Multiple foci

The generation of multiple discrete foci was investigated next. In this case the target was a square array of evenly spaced points. The points were distributed over a

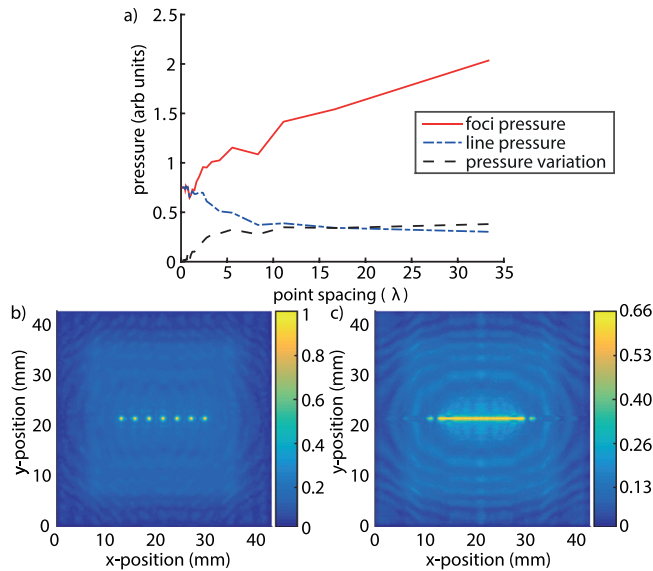


FIG. 7. (Color online) (a) Variation in mean line pressure, mean focal pressure, and standard deviation in pressure over the line with the spacing of points used in discretizing the line measured in simulation. (b) Maximum pressure in target plane of line for a hologram generated using a point spacing of 5.55λ . (c) Maximum pressure in target plane of line for a hologram generated with a point spacing of 0.1675λ . Pressure normalized relative to maximum in (b).

$1\text{ cm} \times 1\text{ cm}$ area centered on the hologram in a plane 3.33 cm away. The number of target points in the array was varied from 2×2 to 11×11 . The variation in the average area occupied by each foci, and the contrast between the target focal points and the background are shown in Fig. 8. To evaluate the average area occupied by each focus the maximum pressure data was interpolated onto a denser grid to improve differentiation, then thresholded at 50%. The area was then given by the size of the cluster centered on each target point in the 2-D target plane.

Figures 8(b) and 8(c) show that arrays of points with evenly distributed pressures can be generated. However, there are several limitations. As the number of points in the array increases, the ratio between the pressure at each target point and the background pressure decreases [Fig. 8(a)]. This is due to both the background pressure increasing and the pressure at each focal point decreasing. For the 11×11 array there is only a 16% difference between the two.

As the number of points in the array increases, the average area occupied by each focus increases gradually until the 8×8 array [Fig. 8(a)]. A 46% increase is seen between the 2×2 and 8×8 arrays. From the 9×9 array onward the pressure at background exceeds 50% of the pressure at the foci. This results in the effective “area” occupied by each focus significantly increasing as different focal points cannot be separately resolved by the metric. The lowest spacing of discrete points that can be achieved is therefore limited to 2.2λ . Note this is distinct from the 0.75λ found in Sec. III C, which represents the maximum discrete point spacing which generates a continuous acoustic pressure.

The MAP of the hologram field perpendicular to the target and hologram planes for the 5×5 array is shown in Fig. 8(d), where the target plane is indicated by the dotted line. It

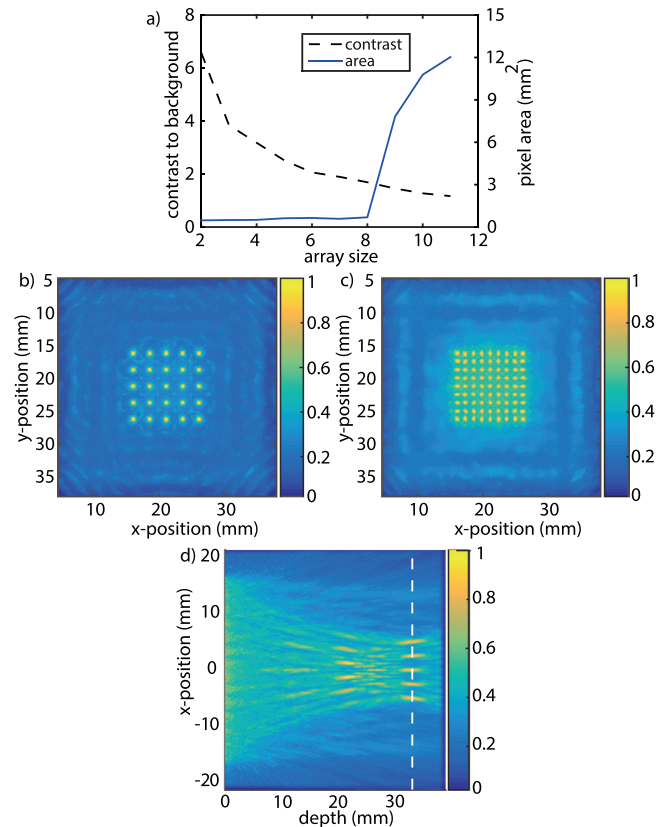


FIG. 8. (Color online) (a) Simulated variation in the ratio of average of the maximum pressure at each focus to the average of the maximum pressure over background pixels as the size of the array increases. Also shown is variation in average area occupied by each focus as the size of the array increases. (b) Maximum pressure in target plane of hologram for a 5×5 array of points (c) Maximum pressure in target plane for a 9×9 array of points. (d) MAP of maximum pressure generated by hologram in (x, z) plane. The dash line indicates target plane for array of foci.

can be seen that high pressure foci are generated in planes other than the target plane. This is a potential drawback. However, these focal points occur in the near field for the hologram aperture, so are not dissimilar to those that occur for conventional piezoelectric arrays.

E. Effect of harmonics on multi-foci field

The simulations in Secs. III C and III D were carried out at a single frequency, pulsed, but without including the contribution from harmonics. This can be a valid approximation, for example, for high frequency holograms in highly attenuating media. However, for most applications their effect needs to be considered. To investigate, the acoustic field generated by the hologram in Fig. 5(c) was simulated again including the contribution from the first two harmonics. The resulting field is plotted in Fig. 9(b).

The introduction of harmonics causes the pressure to vary significantly from the intended distribution. This means for applications at lower frequencies where the number of harmonics could be >10 , the single frequency approximation used in the optimization model is invalid. To account for this, a model-based approach using k-Wave was adopted. First, a forward simulation is run. The input to this

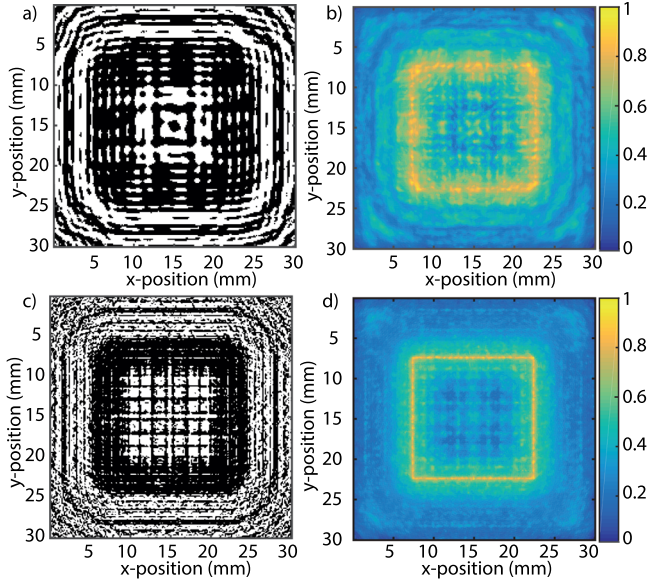


FIG. 9. (Color online) (a) Binary hologram to generate square outline, also displayed in Fig. 5(c). (b) Maximum pressure generated by hologram in (a) in target plane of square, simulated including first two harmonics. (c) Hologram generated using the harmonic corrected forward model from Eq. (8). Target and parameters are identical to (a). (d) Maximum pressure generated by hologram in (c) in target plane of square, simulated including first two harmonics.

simulation is a single hologram pixel in the center $(0, 0)$ of the intended hologram. The temporal input to this pixel matches the source used in the final simulation and can have any number of harmonics. The simulation records the pressure across the target plane of the hologram. This gives the pressure $p_{\text{pixel}}(x, y, t)$ generated by a single hologram pixel at each time point t at each coordinate in (x, y) in the target plane. A time interval covering one period of the pulsing frequency is selected from the pressure data. The pressure $p_{\text{point}}(x, y, t)$ generated at a target point at (x, y) in the target plane by a pixel (i, j) in a $N \times N$ hologram centered on $(0,0)$ is then given by

$$p_{\text{point}}(x, y, t) = p_{\text{pixel}}\left(i - \frac{x}{dx} - \frac{N+1}{2}, j - \frac{y}{dy} - \frac{N+1}{2}, t\right), \quad (7)$$

where dx and dy are the grid spacings in the x and y planes, respectively. For (x, y) coordinates between the simulation grid points, the pressure is calculated by linear interpolation. The overall pressure generated by a given hologram at each target point can then be evaluated using

$$p_{\text{point}}(x, y, t) = \sum_{j=1}^N \sum_{i=1}^N H(i, j) \times p_{\text{pixel}}\left(i - \frac{x}{dx} - \frac{N+1}{2}, j - \frac{y}{dy} - \frac{N+1}{2}, t\right). \quad (8)$$

Here $H(i, j)$ is the current value of the (i, j) th pixel in the hologram. The optimization then proceeds as before over the maximum pressure $\max(p_{\text{point}}(x, y, t))$ generated at each

target point. The algorithm can be extended to points in multiple planes by recording over several planes in the forward simulation.

This model was applied to the same test of generating the outline of a square described in Sec. III A. The resulting hologram and maximum pressure are plotted in Figs. 9(c) and 9(d). It can be seen that the outline of the square is successfully recovered, and that the signal to noise at the target points relative to the background is comparable to that in Fig. 5(d). So, the spectral difference introduced by utilizing a series of short pulses can be accounted for by adjustment of the forward model. However, the hologram generated by this algorithm [Fig. 9(c)] is significantly more speckly than the corresponding hologram in Fig. 9(a). This makes fabrication of these holograms more challenging. However, these regions can be removed from the hologram without a significant alteration to the resulting acoustic field.

IV. PATTERNED ABSORBER FIELD MEASUREMENTS

A. Absorber fabrication and optical source

Experimental measurements were carried out to validate the accuracy of the numerical model and demonstrate that the acoustic fields generated by binary amplitude holograms can be realized experimentally. A set of holographically patterned absorbers were fabricated, and the acoustic field photoacoustically excited from these absorbers by a pulsed laser was measured. Each absorber was fabricated on a $50 \text{ mm} \times 30 \text{ mm} \times 5 \text{ mm}$ transparent PMMA substrate. These were spray painted with a thin layer of black spray paint (Super Satin, Plasti Kote, Valspar). A laser cutter (VLS4.60, Universal Laser Systems) was used to etch the calculated binary holograms from the painted slides.

A Litron Nano L-200 laser (Litron, Rugby, England) was used to generate ultrasound from the fabricated absorbers. This consisted of two Q-switched lasers with spatially coincident beams that could be independently triggered. Both lasers had a wavelength of 1064 nm, a pulse length of 6–9 ns, and a repetition rate of 15 Hz.

B. Two-pulse measurements

An assumption made in the numerical experiments is that there is no variation in the magnitude or shape of the acoustic signal generated by the absorber when two or more optical pulses are incident on it in with a very small timing gap ($< \mu\text{s}$). The validity of this assumption for the absorbers in this experiment was tested.

The experiments were carried out in a $22 \text{ cm} \times 40 \text{ cm} \times 28 \text{ cm}$ plastic tank. An unpatterned absorber fabricated as described in Sec. IV A was attached to the side. The laser was aligned with the absorber and expanded using a 40 mm concave lens to a width of $\sim 2.5 \text{ cm}$. The pulse energy of both Litron lasers was set to 7 mJ. The generated acoustic signals were recorded using a focused polyvinylidene fluoride (PVDF) transducer (Precision Acoustics, Dorchester, UK), which had a center frequency of 25 MHz, and a focal length of approximately 24 mm. The hydrophone was suspended within the tank approximately 2 cm behind the

absorber. Both lasers were externally triggered, and the delay between the two was varied between 0.02 and $2\ \mu\text{s}$. For each delay, three measurements were taken, one where both lasers were triggered together and two where the lasers were used by themselves. Signals were recorded using a digital oscilloscope with a sampling rate of 400 MHz and 256 averages. The bias voltage was removed from each dataset and the single laser measurements were summed accounting for the trigger delay.

Figure 10 shows the recorded voltage from the two pulse and combined single pulse measurements where the trigger delay was $0.5\ \mu\text{s}$. It can be seen that there is no significant variation in magnitude in the second pulse between the two measurements (the correlation coefficient between the two signals was 0.989). This was found to be the case for separations down to 20 ns, on the order of the pulse width, so the assumptions of the numerical model are valid up to frequencies of at least 50 MHz using conventional Q-switched lasers.

C. Patterned absorber field measurements

Acoustic field measurements were taken from two patterned absorbers. The samples used were a hologram with a single focus and a hologram with a focus over a line. Both holograms had aperture sizes of $30\ \text{mm} \times 30\ \text{mm}$, and were designed for a PRF of 3 MHz using a pixel spacing of 0.25 mm. For the hologram with the single focus, the focus was 3 cm from the hologram aperture and placed on the central hologram axis. For the hologram with a line focus, the target was a 20 mm line located 3 cm from the hologram, the line was centered on and parallel to the hologram plane. To calculate the hologram the line was discretized into 400 points. The harmonic corrected algorithm was used accounting for frequencies up to 15 MHz. Clusters of pixels on the hologram smaller than 15 were removed prior to fabrication, as these were not well realized by the laser cutter.

For each measurement the first of the two lasers within the Litron Nano L-200 was used to excite the absorbers. The energy was set to $\sim 300\ \text{mJ}$ per pulse. Measurements of the acoustic field were performed in a $40\ \text{cm} \times 40\ \text{cm} \times 60\ \text{cm}$ tank with a two axis computer controlled positioning system (Precision Acoustics, Dorchester, UK). A calibrated PVDF needle hydrophone with a 0.2 mm active element, different

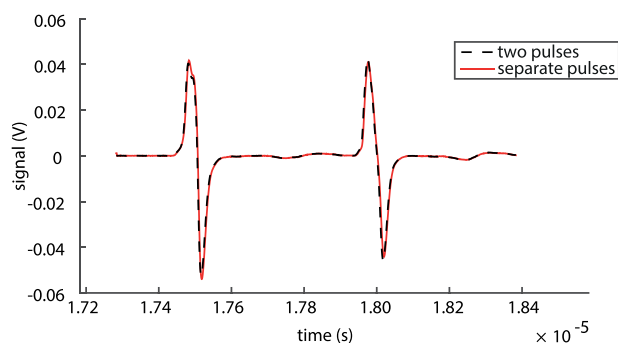


FIG. 10. (Color online) Voltage recorded on hydrophone from two pulse experiment with delay between pulses set to $0.5\ \mu\text{s}$. The red dotted line is the data with both pulses incident on the absorber. The black solid line is the combined data from both lasers used individually with the appropriate delay added back in.

from the transducer used in Sec. IV B, was used to record the pressure (Precision Acoustics, Dorchester, UK).

The laser was positioned 50 cm from the tank edge. A concave lens with a 40 mm focal length was placed 30 cm from the laser to expand the beam. The radius of the beam at the edge of the tank was $\sim 30\ \text{mm}$. The absorber was suspended 30 mm inside the edge of the tank, and was aligned with the laser beam. The needle hydrophone was suspended $\sim 7\ \text{mm}$ away from the absorber and aligned with its center. Signals were recorded over a $30\ \text{mm} \times 30\ \text{mm}$ plane parallel to the absorber using a step size of 0.3 mm. At each position, time domain signals were recorded using a digital oscilloscope with a sampling rate of 400 MHz, taking six averages. A photo of a similar set-up may be found in a previous work.²¹

The Q-switched laser was unable to produce a train of pulses at the desired 3 MHz repetition rate. So, 15 additional pulses were created in the time domain signals. This was done by adding the data recorded at each point to itself translated by multiples of $0.33\ \mu\text{s}$. This temporal spacing corresponds to a 3 MHz pulsing frequency.

To calculate the 3-D wavefield of the hologram from each set of planar measurements, k-Wave was used to forward and back propagate the data. Prior to this, each dataset was spatially up-sampled to a grid spacing of 0.0375 mm to support frequencies up to 20 MHz in the simulation, low pass filtered at 15 MHz to give a minimum PPW of 2.666. The data were also temporally down-sampled to a step size of 7 ns. The single focus hologram measurements were additionally high pass filtered at 100 kHz, and linear acoustic propagation was assumed.

D. Single focus hologram results

For the single focus hologram, the planar measurements were forward and back propagated by 100 and 20 mm, respectively. The resulting field was compared to a numerical simulation run using the same hologram and grid. The MAP of the 3-D field from both the experimental data and the simulation data is shown in Figs. 11(a) and 11(b). The two show good agreement. Both acoustic fields are focused at four distinct points along the central hologram axis, and each foci occurs at approximately the same depth in both sets of data.

The first foci in the field is the design focus, the second is the third order focus of the fourth harmonic, and the third and fourth are generated by the second and third harmonics, respectively. This is confirmed by the spectra measured at each focus [Figs. 11(c)–11(f)]. The frequency with the maximum amplitude in the spectra matches the predicted harmonic for the second, third, and fourth foci in both the simulation and experimental data [Figs. 11(d)–11(f)]. At the design focus the third harmonic has a higher amplitude than the fundamental in both spectra [Fig. 11(c)]. This is because, as discussed in Sec. II C, the third order focus for the third harmonic also occurs at this point.

The peak pressure measured at the design focus in the experiment was 187.3 kPa. The maximum pressure in the data that was propagated was 79.8 kPa giving a focal gain of

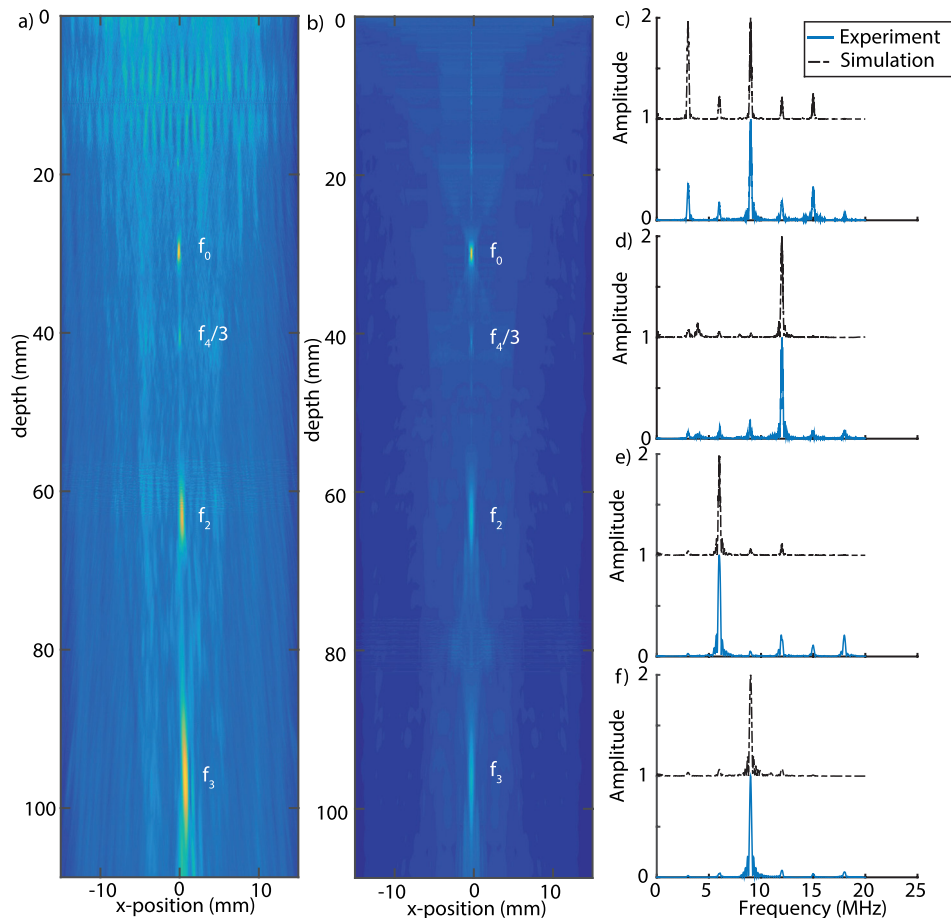


FIG. 11. (Color online) Comparison between the MAPs of the maximum pressure fields produced from the single focus hologram (a) simulation and (b) experiment. In both projections the hologram is located along the top image axis. Positions of the foci of different harmonics are labeled. (c)–(f) Spectra measured at each of the focal points labeled in (a) and (b). Each spectra is normalized to its maximum. Simulation spectra is offset by 1 in each case relative to experiment.

2.347. However, this represents only the spectral content up to 15 MHz. The peak pressure in the experimental data up to the 30 MHz to which the needle hydrophone was calibrated was 326 kPa. Assuming equivalent focal gain this gives a pressure of 764.17 kPa at the focus. This could be further improved by the use of a optimized absorber over black spray paint.³ The pressure achieved is over an order of magnitude higher than pressures reported in previous works utilizing longer modulated pulses as the optical source.¹⁸

E. Line focus hologram results

For the hologram with a line focus, the planar measurements were forward and back propagated by 30 and 20 mm,

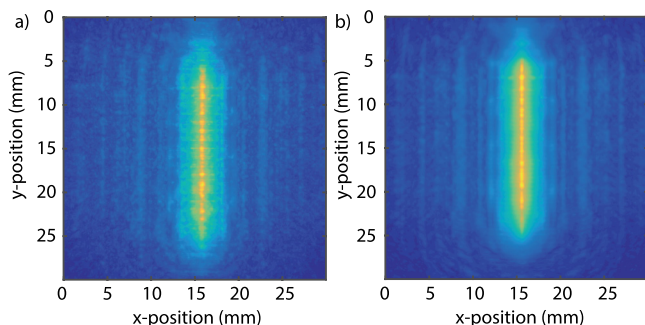


FIG. 12. (Color online) (a) Maximum pressure in the target plane of line for the line focus hologram recorded in experiment. (b) Maximum pressure in target plane of the line for the line focus hologram simulated using k-Wave correcting for the spatial profile of laser using experimental data.

respectively. The plane of the hologram was found in the back propagated data, and the target line was then identified 30 mm from this hologram plane. This was compared against a simulation of the acoustic field generated by the same hologram. The spatial profile of the laser was accounted for in this simulation by registering the maximum pressure in the hologram plane of the back propagated data to the calculated hologram, then using this registered maximum pressure as the spatial profile in the forward simulation.

It can be seen from Fig. 12(a) that a line focus is generated by the fabricated hologram. The peak pressure over the line is 91.6 kPa. The experiment and the simulation show good agreement [Fig. 12(b)] demonstrating that acoustic fields focused over patterned distributions can be generated using binary amplitude holograms and that the field generated by these holograms can be accurately modeled using the k-Wave toolbox. In the future, the optimization approach adopted in this work could be further adapted to include the spatial profile of the beam by introducing a weighting factor for the different hologram pixels.

V. SUMMARY AND CONCLUSION

This study has demonstrated numerically and experimentally that acoustic fields focused over patterns, at multiple discrete points, or at single points in three dimensions can be generated using the photoacoustic effect. This is achieved by the application of multiple high peak-power

optical pulses to a binary amplitude hologram, at the holograms design frequency. The use of a high peak-power optical pulses facilitates the generation of patterned fields with greater acoustic pressures than alternative modulated sources. The harmonics that this source introduces into the acoustic pulse spectrum can be accounted for in the calculation of the binary holograms.

There are currently a number of obstacles to the application of this approach to practical problems. The generation of multiple high peak power optical pulses with a high repetition rate requires either the use of several Q-switch lasers triggered in sequence or a mode-locked Q-switched laser,¹⁹ and both these options are expensive. However, this could be overcome in the future by using high power high repetition rate fiber and diode lasers currently being developed.²⁸

Creating the hologram by patterning an absorbing layer also has two practical limitations. First, each hologram can only generate a single design acoustic field, at a single frequency (for multi-focal patterns), making the holograms inflexible. Second, each pattern possesses gaps resulting in a portion of the incident optical radiation being transmitted into the medium, potentially generating unwanted photoacoustic signals. In future work, the patterned absorber could be replaced by a SLM.¹⁸ This can modulate the light field incident on a uniform absorber, such that ultrasound is excited from only part of the absorber. This would allow for rapid variation of the generated acoustic fields and prevent the transmission of light into the surrounding medium.

ACKNOWLEDGMENTS

The authors would like to thank the EPSRC for funding the work and Litron for the use of the Litron Nano L-200. J.J. is financed from the SoMoPro II Programme, co-financed by the European Union and the South-Moravian Region. This work reflects only the authors' view and the European Union is not liable for any use that may be made of the information contained therein. Computational resources were provided by the IT4Innovations excellence in science project (IT4I XS - LQ1602).

¹P. Beard, "Biomedical photoacoustic imaging," *Interface Focus* **1**, 602–631 (2011).

²T. Buma, M. Spisar, and M. O'Donnell, "High-frequency ultrasound array element using thermoelastic expansion in an elastomeric film," *Appl. Phys. Lett.* **79**, 548–550 (2001).

³H. W. Baac, J. G. Ok, H. J. Park, T. Ling, S. Chen, A. J. Hart, and L. J. Guo, "Carbon nanotube composite optoacoustic transmitters for strong and high frequency ultrasound generation," *Appl. Phys. Letters*, **97**, 234104 (2010).

⁴B. E. Treeby, B. T. Cox, E. Z. Zhang, S. K. Patch, and P. C. Beard, "Measurement of broadband temperature dependent ultrasonic attenuation and dispersion using photoacoustics," *IEEE Trans. Ultrason. Ferroelectr. Freq. Control* **56**, 1666–1676 (2009).

⁵Y. Hou, J. Kim, S. Ashkenazi, S. Huang, L. J. Guo, and M. O'Donnell, "Broadband all-optical ultrasound transducers," *Appl. Phys. Lett.* **91**, 073507 (2007).

⁶A. I. H. Chen, L. L. P. Wong, and J. T. W. Yeow, "Recent advances in capacitive micromachined ultrasonic transducer imaging systems," in *Medical Imaging: Technology and Applications*, edited by T. Farncombe and K. Iniewski (CRC Press, Taylor and Francis Group, Boca Raton, FL, 2014), Chap. 10, pp. 253–270.

⁷C. Sheaff and S. Ashkenazi, "A polyimide-etalon thin film structure for all-optical high-frequency ultrasound transduction," *IEEE Trans. Ultrason. Ferroelectr. Freq. Control* **59**, 2254–2261 (2012).

⁸S. Dixon, T. Harrison, Y. Fan, and P. A. Petcher, "Thermoelastic laser generated ultrasound using a ring source," *J. Phys. D: Appl. Phys.* **45**, 175103 (2012).

⁹P. Cielo, F. Nadeau, and M. Lamontagne, "Laser generation of convergent acoustic waves for materials inspection," *Ultrasonics* **23**, 55–62 (1985).

¹⁰S. Zamiri, B. Reitingner, S. Bauer, and P. Burgholzer, "Converging laser generated ultrasonic waves using annular patterns irradiation," *J. Phys. Conf. Ser.* **520**, 012001 (2014).

¹¹G. Cachier, "Optical excitation of high-amplitude surface waves," *Appl. Phys. Lett.* **17**, 419–420 (1970).

¹²H. Nishino, Y. Nagata, T. Koda, K. Yamanaka, and Y. Tsukahara, "Excitation of high frequency surface acoustic waves by phase velocity scanning of a laser interference fringe," *Appl. Phys. Lett.* **62**, 2036–2038 (1993).

¹³A. Arca, J. Aylott, L. Marques, M. Clark, M. Somekh, R. Smith, S. Sharples, T. Stratoudaki, and X. Chen, "CHOTs optical transducers," *Nondestruct. Testing Eval.* **26**, 353–366 (2011).

¹⁴I. J. Collison, T. Stratoudaki, M. Clark, and M. G. Somekh, "Measurement of elastic nonlinearity using remote laser ultrasonics and cheap optical transducers and dual frequency surface acoustic waves," *Ultrasonics* **48**, 471–477 (2008).

¹⁵T. Stratoudaki, M. Clark, M. Somekh, and A. Arca, "Cheap optical transducers (CHOTs) for generation and detection of longitudinal waves," in *IEEE International Ultrasonics Symposium* (2012), pp. 961–964.

¹⁶J. B. Deaton, Jr., A. D. W. McKie, J. B. Spicer, and J. W. Wagner, "Generation of narrow-band ultrasound with a long cavity mode-locked Nd:YAG laser," *Appl. Phys. Lett.* **56**, 2390–2392 (1990).

¹⁷C. M. Grunsteidl, I. A. Veres, T. Berer, and P. Burgholzer, "Application of SLM generated patterns for laser-ultrasound," in *IEEE International Ultrasonics Symposium* (2014), pp. 1360–1363.

¹⁸A. Meyer, S. Gspan, S. Bernet, and M. Ritsch-Marte, "Tailoring ultrasonic beams with optoacoustic holography," *Proc. SPIE Laser Resonators Beam Control VI* **4969**, 105–114 (2003).

¹⁹S. D. Sharples, M. Clark, and M. G. Somekh, "All-optical adaptive scanning acoustic microscope," *Ultrasonics*, **41**, 295–299 (2003).

²⁰S. Gspan, A. Meyer, S. Bernet, and M. Ritsch-Marte, "Synthetic acoustic holograms realised via optoacoustic methods," *Proc. SPIE Photons Ultrasound* **5697**, 99–106 (2005).

²¹M. D. Brown, T. J. Allen, B. T. Cox, and B. E. Treeby, "Control of optically generated ultrasound fields using binary amplitude holograms," in *IEEE International Ultrasonics Symposium* (2014), pp. 1037–1040.

²²B. E. Treeby and B. T. Cox, "k-Wave: MATLAB toolbox for the simulation and reconstruction of photoacoustic wave-fields," *J. Biomed. Opt.* **15**, 021314 (2010).

²³J. Jaros, A. P. Rendell, and B. E. Treeby, "Full-wave nonlinear ultrasound simulation on distributed clusters with applications in high-intensity focused ultrasound," *Int. J. High Performance Comput. Appl.* 1–19 (2015).

²⁴G. W. Webb, I. V. Minin, and O. V. Minin, "Variable reference phase in diffractive antennas: Review, applications, new results," *Antennas Propag. Mag.* **53**, 77–94 (2011).

²⁵P. Tsang, T. C. Poon, W. K. Cheung, and J. P. Liu, "Computer generation of binary Fresnel holography," *Appl. Opt.* **50**, 88–95 (2011).

²⁶M. Clark, "A direct search method for the computer design of holograms," Ph.D. thesis, Imperial College, London, UK, 1997.

²⁷M. A. Seldowitz, J. P. Alleback, and D. W. Sweeney, "Synthesis of digital holograms by direct binary search," *Appl. Opt.* **26**, 2788–2798 (1987).

²⁸D. J. Richardson, J. Nilsson, and W. A. Clarkson, "High power fibre lasers: Current status and future perspectives [Invited]," *J. Opt. Soc. Am. B* **27**, B63–B92 (2010).